

Topology driven quantum phase transitions in time-reversal invariant anyonic quantum liquids

Charlotte Gils,¹ Simon Trebst,² Alexei Kitaev,³ Andreas W. W. Ludwig,⁴ Matthias Troyer,¹ and Zhenghan Wang²

¹Theoretische Physik, ETH Zurich, 8093 Zurich, Switzerland

²Microsoft Research, Station Q, University of California, Santa Barbara, CA 93106

³Institute for Quantum Information, California Institute of Technology, Pasadena, CA 91125

⁴Physics Department, University of California, Santa Barbara, CA 93106

(Dated: February 12, 2022)

Indistinguishable particles in two dimensions can be characterized by anyonic quantum statistics more general than those of bosons or fermions. Such anyons emerge as quasiparticles in fractional quantum Hall states and certain frustrated quantum magnets. Quantum liquids of anyons exhibit degenerate ground states where the degeneracy depends on the topology of the underlying surface. Here we present a novel type of continuous quantum phase transition in such anyonic quantum liquids that is driven by quantum fluctuations of topology. The critical state connecting two anyonic liquids on surfaces with different topologies is reminiscent of the notion of a ‘quantum foam’ with fluctuations on all length scales. This exotic quantum phase transition arises in a microscopic model of interacting anyons for which we present an exact solution in a linear geometry. We introduce an intuitive physical picture of this model that unifies string nets and loop gases, and provide a simple description of topological quantum phases and their phase transitions.

Phases of matter can exhibit a vast variety of ordered states that typically arise from spontaneous symmetry breaking and can be described by a local order parameter. A more elusive form of order known as ‘topological order’¹ reveals itself through the appearance of robust ground-state degeneracies, but cannot be described in terms of a local order parameter. Examples of such topological quantum liquids are the fractional quantum Hall states² where the ground-state degeneracy depends on the number of ‘antidots’ which can be viewed as punctures (holes) in the two-dimensional surface populated by the quantum Hall liquid³. It has long been proposed that topological quantum liquids also occur in certain frustrated quantum magnets^{4,5,6,7,8,9}, but it has only been in recent years that strong candidate materials have emerged^{10,11}. While quantum Hall liquids break time-reversal symmetry, the exotic ground states of frustrated quantum magnets are expected to preserve time-reversal symmetry. As a consequence of this symmetry many unexplored phenomena may appear, including the intriguing possibility of topology driven quantum phase transitions which is the central aspect of this manuscript.

In this manuscript we develop an intuitive physical picture for the emerging low energy physics of topological quantum liquids and their phase transitions in terms of surfaces and their topology. We thereby provide a visualization of the underlying quantum physics, which is in one-to-one correspondence to a detailed analytical framework. Here we consider systems that preserve time-reversal symmetry which in this picture will be described by quantum liquids on closed surfaces. Such liquids exhibit ground-state degeneracies that depend (exponentially) on the genus of the surface. A section of an extended high-genus surface formed by a triangular arrangements of ‘holes’ is shown in Fig. 1. Through every such hole there can be a flux of the liquid populating the surface. An exponential degeneracy then arises from the possible flux assignments through the holes. While in the presence of a flux a hole cannot be contracted, we can eliminate the hole in the absence of flux without changing the state of the topological liquid. If there is no flux through any of the holes, they can all be removed, and the state of the quantum liquid is identical to that on two separated sheets, as shown on the left side in Fig. 1. It is this state that exhibits topological order. On the other hand, if there is no flux through the tubes in the interior of the surface (centered around the black lines in Fig. 2), we can

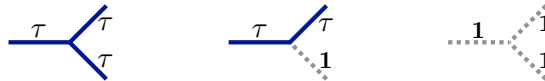


FIG. 1: *Phase transition in two dimensions.* Two-dimensional surfaces with different topologies that are populated by anyonic quantum liquids. A quantum phase transition driven by fluctuations of the surface topology connects the anyonic liquid on two separated sheets (on the left) and decoupled spheres (on the right).

pinch them off. The resulting state of the quantum liquid is then identical to that of disconnected spheres, as shown on the right side in Fig. 1. This state has neither ground-state degeneracy nor topological order.

Here we will introduce a microscopic model which energetically favors the absence of flux through the holes or tubes, thus dynamically implementing the two topology changing processes mentioned above. The competition of the two processes drives a quantum phase transition between the two extreme states. Our model is defined on the ‘skeleton’ that surrounds the holes in the interior of the surface as illustrated in Fig. 2 where the skeleton forms a honeycomb lattice. The fluxes in the tubes are associated with discrete degrees of freedom on the edges of the skeleton lattice, corresponding to anyonic particles of the quantum liquid¹². The set of degenerate ground states of the liquid is now in one-to-one correspondence with all labelings of the edges consistent with a given set of constraints, characteristic to the underlying quantum liquid.

As a simple example, we consider a quantum liquid of so-called Fibonacci anyons^{13,14,15}. Here there are only two possible labelings, namely the trivial particle $\mathbf{1}$ and the Fibonacci anyon τ . At any trivalent vertex of the skeleton lattice, there is a constraint forbidding the appearance of only a single τ -anyon on the three edges connected to the vertex, allowing the following possibilities:



Due to this constraint the edges occupied by a τ -anyon form a closed, trivalent net known as a ‘string net’⁷. One might as well identify the two degrees of freedom ($\mathbf{1}, \tau$) with the two states of a spin-1/2 (\uparrow, \downarrow) and thus the same states can be viewed as representing the ground states of a Hamiltonian with three-spin interactions enforcing the vertex constraint above (no single \downarrow -spin around a vertex)¹⁶.

Returning to our model, we can now specify its microscopic terms

$$H = -J_e \sum_{\text{edges } e} \delta_{\ell(e), \mathbf{1}} - J_p \sum_{\text{plaquettes } p} \delta_{\phi(p), \mathbf{1}}. \quad (1)$$

The first term favors a trivial label $\ell(e) = \mathbf{1}$ on the edge e corresponding to the no-flux state. The second term favors the no-flux state $\phi(p) = \mathbf{1}$ for the plaquette p . When expressed in terms of the labels $\ell(e)$, the plaquette flux $\phi(p)$ is a complicated, but local expression involving the twelve edges connected to the vertices surrounding a plaquette, see Fig. 2, and is explicitly given in the supplementary material. In the absence of the first term ($J_e = 0$) the plaquette term will effectively close all holes, and the ground state of the above Hamiltonian describes that of the quantum liquid on two parallel sheets as illustrated in Fig. 1. The latter is precisely the string-net model first introduced by Levin and Wen⁷, which is also closely related to another model of string nets discussed recently by Fendley¹⁷. Similarly, in the absence of the plaquette term, $J_p = 0$, the edge term with coupling constant J_e will close off all the ‘tubes’ thus leading to the ground state of the quantum liquid on multiple disconnected spheres as illustrated in Fig. 1. This edge term acts as a string tension in the string net model, or as a magnetic field in its spin model representation.

In the presence of both terms in the Hamiltonian, quantum fluctuations are introduced which correspond to fluctuations of the surface. These fluctuations are virtual processes where plaquettes or tubes close off and open depending on the flux through them. We can visualize these fluctuations as local changes to the genus of the surface. If the two terms in the Hamiltonian become comparable in strength, the competition between the two drives a quantum phase transition between the two extremal topologies (see Fig. 1). At this quantum phase transition the fluctuations of the surface become critical and *the topology of the surface fluctuates* on all length scales. We can visualize the (imaginary) time-evolution of this quantum critical state as a

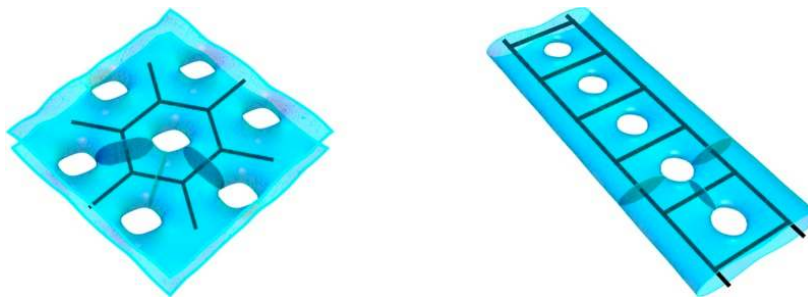


FIG. 2: *Microscopic model.* Our microscopic model energetically favors the flux-free states for the holes and tubes (shaded) of the illustrated two-dimensional surfaces. For the surface with a triangular arrangement of holes shown in the left panel the anyonic degrees of freedom in our model are associated with the edges of the honeycomb lattice skeleton that surrounds the holes in the interior of the surface. For the linear geometry of holes on the right the skeleton lattice forms a ladder geometry.

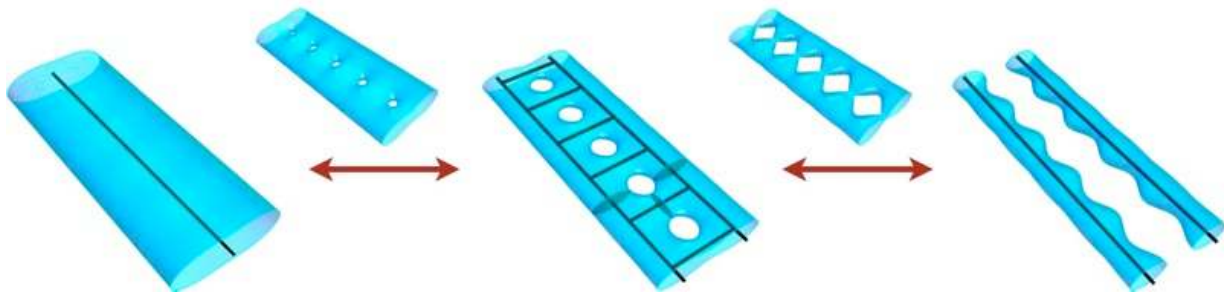


FIG. 3: *Phase transition in one dimension.* Illustration of the quantum phase transition driven by fluctuations of the surface topology in a linear geometry which connects the extreme limits of a ‘single cylinder’ (on the left) and ‘two cylinders’ (on the right).

‘foam’ in space-time, which is reminiscent of the notion of a quantum foam introduced by John Wheeler for fluctuations of 3+1 dimensional Minkowski space at the Planck scale^{18,19}.

To understand the nature of this transition, we first focus on the linear geometry shown in Fig. 2. In this geometry the Hamiltonian becomes

$$H = -J_r \sum_{\text{rungs } r} \delta_{\ell(r),1} - J_p \sum_{\text{plaquettes } p} \delta_{\phi(p),1}, \quad (2)$$

where the first term now only acts on the rungs between the holes (i.e. on those edges of the skeleton which separate two neighboring plaquettes), in analogy to the original model. This model exhibits a *continuous* quantum phase transition between the two extreme topologies shown in Fig. 3. This continuous transition is driven by fluctuations of topology. It turns out that the gapless theory describing this transition can be *solved exactly* as discussed in more detail below and explicitly in the supplementary material.

The two extreme topologies connected by this transition in the linear geometry are as follows: In the limit of a vanishing rung term, $J_r = 0$, the ground state is that of an anyonic quantum liquid on a single cylinder where all the plaquettes are closed, as shown on the left in Fig. 3. For Fibonacci anyons this ground state is two-fold degenerate, with either a τ -flux or no flux through the cylinder. In the opposite limit of vanishing plaquette term, $J_p = 0$, we can close off all the rungs and the ladder splits into two separate cylinders with a four-fold ground state degeneracy (either a τ -flux or no flux in either of the cylinders), as shown on the right in Fig. 3.

In both limits excitations above these ground states are gapped quasiparticles with a gap of J_p or J_r , respectively. The first excited state above the ‘single cylinder’ ground state is a τ -flux threading a single plaquette, which prevents it from being closed as illustrated in Fig. 4a). In the opposite limit of the ‘two cylinder’ ground state the first excited state is a τ -flux through one of the rungs, leaving this rung connecting the two cylinders as shown in Fig. 4b). Turning on a small coupling $J_r \neq 0$, or $J_p \neq 0$ respectively, these excitations delocalize, but remain gapped and form bands in the energy spectrum, as explicitly displayed in Fig. 5a). For large couplings, some of these excitations proliferate and their gap vanishes at the quantum phase transition mentioned above.

The full phase diagram is shown in Fig. 5b), where we parameterize the two couplings on a circle as $J_p = \cos \theta$ and $J_r = \sin \theta$. Positive (negative) coupling constants indicate that the no-flux (τ -flux) states are energetically favored and the two extreme limits discussed above then correspond to the points $\theta = 0$ and $\theta = \pi/2$ on the circle. The continuous phase transition between these two distinct topologies occurs for equal positive coupling strengths $J_r = J_p$, which corresponds to the point $\theta = \pi/4$ on the circle.

We can visualize this critical point as a quasi one-dimensional quantum foam, with topology fluctuations of the surface on all length scales. As a first step, we have performed a detailed numerical analysis of this critical point using exact diagonalization of systems with up to 36 anyons. The continuous nature of the phase transition reveals itself in a linear energy-momentum dispersion relation, which is indicative of conformal invariance. A detailed analysis of the energy spectrum further allows to

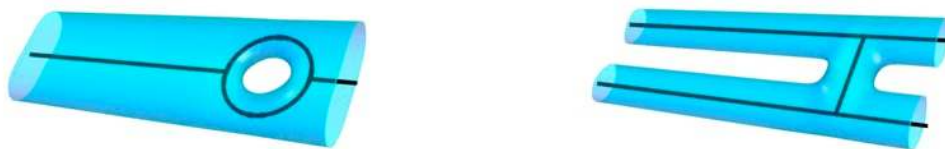


FIG. 4: *Excitations.* Plaquette (left) and rung (right) excitations above the two extreme ground states illustrated in Fig. 3.

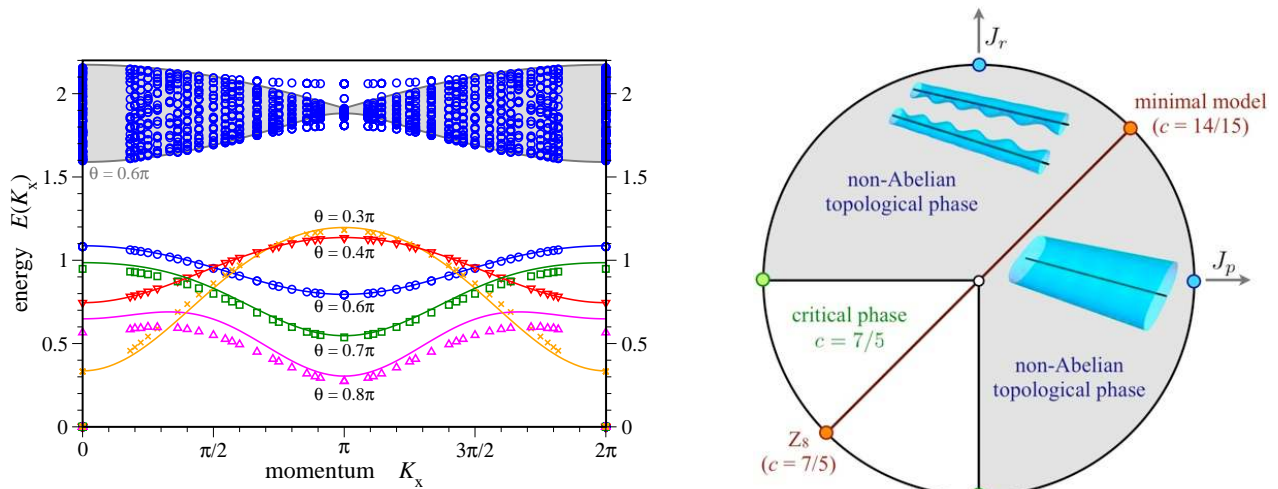


FIG. 5: *Left: Energy spectra.* Energy spectra of our microscopic model near the decoupling point ($\theta = \pi/2$). The rung excitations shown in Fig. 4 form a gapped quasiparticle band well below a continuum of states (shaded). Open symbols show results from exact diagonalization of systems with 24 to 36 anyons. These bands are well described by second order perturbation theory around the decoupling point shown as solid lines. *Right: Phase diagram.* The phase diagram of our microscopic model (2) where the couplings are parametrized as $J_p = \cos \theta$ and $J_r = \sin \theta$. The gapped topological phases are indicated by the shaded regions. The topology driven quantum phase transition occurs at the exactly solvable critical point $\theta = \pi/4$. An extended critical phase is found in the region $\theta \in (\pi, 3\pi/2)$ around the second solvable (critical) point $\theta = 5\pi/4$.

uniquely identify the corresponding conformal field theory (CFT), which in this case turns out to be the 7th member²⁰ of the famous series of so-called unitary minimal CFTs²² with central charge $c = 14/15$. This particular identification of a conformal field theory is part of a broader scheme which connects the gapless theory of the topology driven phase transition with the nature of the underlying anyonic liquid. In the present case of a quantum liquid of Fibonacci anyons we can make an explicit connection between the (total) quantum dimension of the anyonic liquid and the central charge of the conformal field theory.

In fact, the Hamiltonian at this point is even exactly solvable. The key insight leading to this exact, analytical solution is the observation that the Hamiltonian of our topological model can be mapped precisely onto a particular version of the restricted-solid-on-solid (RSOS) model, which is exactly integrable and directly leads to the above-mentioned CFT²³. This mapping explicitly connects the Hamiltonian at this critical point with an integrable Hamiltonian defined by the Dynkin diagram D_6

$$\begin{array}{c}
 \bullet (1, \tau) \\
 | \\
 \bullet (1, 1) \quad \bullet 1 \quad \bullet (\tau, \tau) \quad \bullet \tau \\
 | \\
 \bullet (\tau, 1)
 \end{array}
 \quad . \quad (3)$$

Here the particular labeling of the Dynkin diagram arises from the underlying topological structure of our model. Specifically the labels describe the topological fluxes in the two extreme limits of the model as illustrated in Fig. 3, with the limit of a ‘single cylinder’ in the picture on the left corresponding to the blue circles in the Dynkin diagram and the limit of the ‘two cylinders’ pictured on the right corresponding to the green circles. This underlying structure also gives rise²⁴ to a representation of the Temperley-Lieb algebra²⁵ which is characterized by the total quantum dimension $d = \sqrt{2 + \phi}$ of the anyonic liquid, where $\phi = (1 + \sqrt{5})/2$ is the golden ratio. A more detailed discussion of the exact solution is given in the methods section and the supplementary material.

Varying the couplings in our Hamiltonian there is another way of connecting the two phases depicted in Fig. 3, which is to change the sign of both couplings in the Hamiltonian. For opposite sign the two terms now favor τ -fluxes through rungs and plaquettes, respectively, which again leads to a competition. Interestingly, we find that this competition results in an *extended*, critical phase separating the two topologically distinct phases, as depicted in the phase diagram of Fig. 5. For the full extent of this critical phase we again have topology fluctuations on all length scales. However, the gapless theory describing this phase turns out to be in a different universality class as compared to the critical point discussed above. These results can again be obtained through a combination of numerical and exact analytical arguments, which are detailed in the supplementary material. In particular, there is another integrable point in this extended critical phase for equal coupling strengths $J_r = J_p$, which corresponds to the angle $\theta = 5\pi/4$ in the phase diagram of Fig. 5, and is thus located exactly opposite of the one discussed above. Following a similar route one can map the Hamiltonian at this second integrable point to another variant of the RSOS

model associated with the Dynkin diagram D_6 . The gapless theory at this point then turns out to be exactly the Z_8 parafermion CFT with central charge $c = 7/5$. The stability of this gapless theory away from the integrable point is due to an additional symmetry of our model^{26,27}. Numerically, we find that it extends throughout the whole region where both couplings favor the τ -flux states all the way to the points $\theta = \pi$ and $\theta = 3\pi/2$, where there is no longer a competition of the two terms of the Hamiltonian and the ground states have fluxes either through all plaquettes or rungs, respectively.

Returning to our original discussion of the model (1) on the surface in Fig. 1, the question arises whether we can understand the nature of the quantum phase transition here as well. We can explicitly address this question in the context of another kind of anyons, the so-called semions²⁸. Again, there are two possible labelings, the trivial particle $\mathbf{1}$ and the semion s . The constraint now only allows zero or two semion particles s at any trivalent vertex. The set of edges carrying a semion s form loops instead of nets and give rise to what is known as a ‘loop gas’^{8,29}. In its spin-1/2 representation (where \uparrow, \downarrow now stand for $\mathbf{1}$ and s) this model is known as the honeycomb version of the toric code⁸, where the string tension J_e corresponds to a magnetic field. This model exhibits a continuous quantum phase transition in the 3D Ising universality class^{30,31} with topology fluctuations on all length scales. Mapping the 2+1 dimensional semion system to its three-dimensional classical counterpart, the quantum foam then corresponds to the critical fluctuations of domain walls in a 3D Ising model at its critical point. For other kinds of anyonic liquids, the nature of the topology changing transition is in general unknown and remains an intriguing open problem with the possibility of new universality classes. For a liquid of Fibonacci anyons there has been a recent discussion of quantum critical behavior by Fendley from the perspective of ground-state wavefunctions and their respective correlators in terms of conformal field theory¹⁷.

Finally, in order to explore the broader context of our models we complete our analysis by considering the complete set of possible excitations present in these models. An excitation different from the ones already discussed arises when relaxing the constraint which for every trivalent vertex of the skeleton lattice forbids the occurrence of a single τ -flux. If we allow for this possibility, we are left with a τ -flux entering the vertex through one tube, but not leaving it through another tube in the skeleton plane as illustrated in Fig. 2. Instead we can think of the remaining τ -flux at such a vertex as leaving through one of the liquid sheets surrounding the skeleton lattice. This piercing of the liquid by a τ -flux corresponds to a vortex excitation of the liquid and is illustrated as a ‘chimney’ in Fig. 6. These vortex excitations break time-reversal symmetry and turn out to all possess the same chirality (indicated by the red arrow in Fig. 6). This is only possible if the anyonic liquid on a given sheet itself possess a given chirality. Since the entire system exhibits time-reversal symmetry, this means that the two anyonic liquids on the two sheets must have opposite chirality. Vortices associated with chimneys on opposite sheets thus also have opposite chirality as illustrated in Fig. 6. (In fact, a vortex in one sheet can be related to a vortex in the opposite sheet by dragging a vortex through a ‘hole’ connecting the two sheets. Moreover, we can create a ‘hole’ connecting the sheets by glueing together two vortex excitations on opposite sheets.) This conceptual perspective of two anyonic liquids with opposite chirality giving rise to a time-reversal invariant model connects with and allows a visualization of a more abstract mathematical description of these models, namely doubled non-Abelian Chern-Simons theories³². It remains an intriguing question to formulate our topology driven phase transitions within such a field theoretical framework.

In this manuscript we have developed a general, unifying framework to formulate topological aspects of quantum states of matter for systems preserving time-reversal symmetry and of their phase transitions. In a simple and intuitive picture they are described in terms of fluctuations of two-dimensional surfaces and their topology changes. Our framework gives a new perspective on how to broadly discuss quantum phase transitions out of topologically ordered states of matter, which has so far been largely unexplored territory due to the lack of a local order parameter description amenable to a Landau-Ginzburg-Wilson theory. This description of time-reversal invariant anyonic quantum liquids is also expected to advance our understanding of

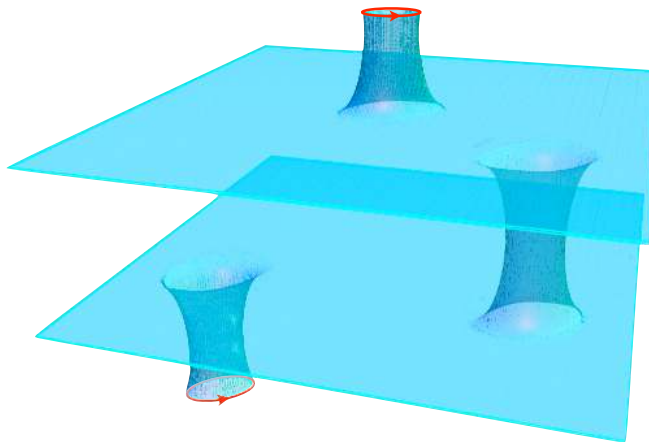


FIG. 6: *Excitations of the anyonic liquid.* Vortex excitations of the liquid indicated by the ‘chimneys’ possess a chiral edge mode.

spin liquid states and their phase transitions in recently proposed materials of frustrated quantum magnetism and other strongly correlated systems. Our unifying perspective on string nets and quantum loop gases will also allow to construct a large variety of new microscopic models for topological phases.

Acknowledgments.— We thank M. Freedman, X.-G. Wen, and P. Fendley for stimulating discussions. Our numerical simulations were based on the ALPS libraries³³. A. W. W. L. was supported, in part, by NSF DMR-0706140.

Methods

Identification of conformal field theories. To characterize the conformal field theory (CFT) of the critical points in the linear (ladder) geometry, we rescale and match the finite-size energy spectra obtained numerically by exact diagonalization for systems with up to $L = 36$ anyons to the form of the spectrum of a CFT,

$$E = E_1 L + \frac{2\pi v}{L} \left(-\frac{c}{12} + h + \bar{h} \right), \quad (4)$$

where the velocity v is an overall scale factor, and c is the central charge of the CFT. The scaling dimensions $h + \bar{h}$ take the form $h = h^0 + n$, $\bar{h} = \bar{h}^0 + \bar{n}$, with n and \bar{n} non-negative integers, and h^0 and \bar{h}^0 are the holomorphic and antiholomorphic conformal weights of primary fields in a given CFT with central charge c . The momenta (in units $2\pi/L$) are such that $k_x = h - \bar{h}$ or $k_x = h - \bar{h} + L/2$. Using this procedure we find that for the critical point at $\theta = \pi/4$ the rescaled energy spectrum matches the assignments (28) of the 7th member²⁰ of the famous series of so-called unitary minimal CFTs²² with central charge $c = 14/15$. Similarly, at the point $\theta = 5\pi/4$ we find the rescaled energy spectrum to match that of the Z_8 parafermion CFT with central charge $c = 7/5$. For the calculated energy spectra and the details of these assignments we refer to the supplementary material.

Exact analytical solution. The Hamiltonian in Eq. (2) can be solved exactly for interaction strengths corresponding to angles $\theta = \pi/4$ and $\theta = 5\pi/4$ in the phase diagram of Fig. 5. This exact, analytical solution of the gapless theories at these points unambiguously demonstrates the continuous nature of the related quantum phase transitions and points to generalizations of these gapless theories for other kinds of anyonic liquids. The key observation underlying this exact solution is the emergence of the D_6 Dynkin diagram from the topology of the surface associated with the ladder model as depicted in the right part of Fig. 2. Each labeling of the edges of the ‘skeleton’ graph which corresponds to that surface, denotes one of the states spanning the Hilbert space of the system. A crucial step is to consider a different ‘pants decomposition’³⁶ of this surface and to perform a *basis change* to a new basis which corresponds to the labeling of the skeleton lattice of this alternative pants decomposition. Explicitly, this basis transformation can be written as

$$= \sum_{c_2, c_4} (F_{b_1 a_1 a_3}^{b_3})_{c_2}^{c_4} (F_{b_3 a_3 a_5}^{b_5})_{d_4}^{c_4}$$

Here, $(F_{bcd}^a)_{a'}^{b'}$ denotes the so-called F -matrix, which is a generalization of the familiar $6j$ symbols of angular momentum coupling in conventional quantum mechanics and is known for any anyonic liquid³⁸. Note that associated with the even-numbered indices of these labels, which correspond to the original rung labels c_i on the right, there is the flux through the cross-section of the surface on the left, denoted by a label $d_i = 1$ or $d_i = \tau$. Similarly, associated with the odd-numbered indices, which correspond to the original plaquettes, there is a *pair* of fluxes through the two cross-sections of the surface at the position of the plaquette on the left, denoted by a *pair of labels*, (a_i, b_i) . This pair of labels can assume four values, i.e., $(a_i, b_i) = \{(1, 1); (\tau, 1); (1, \tau); (\tau, \tau)\}$. The (fusion) constraints at the vertices where the labels (a_i, b_i) and $d_{i\pm 1}$ meet then turn out to be precisely the condition that they be adjacent nodes on the D_6 Dynkin diagram of Eq. (3). For example, a local label $(a_i, b_i) = (\tau, \tau)$ at an odd-numbered index i only allows for labels $d_{i-1} = 1$ and $d_{i+1} = \tau$ at the neighboring even-numbered indices. This is reflected in the Dynkin diagram by the appearance of a line that connects the label (τ, τ) to both labels 1 and τ . The importance of the just described basis change consists in the fact that in the new basis the rung and plaquette terms, H_i^r and H_i^p , respectively, of our ladder Hamiltonian

$$H = -J_r \sum_{i \text{ even}} H_i^r - J_p \sum_{i \text{ odd}} H_i^p, \quad (5)$$

turn out to have precisely the form of a known representation²⁴ of the Temperley-Lieb algebra²⁵ associated with the D_6 Dynkin diagram,

$$\mathbf{e}_i^2 = D \mathbf{e}_i, \quad \mathbf{e}_i \mathbf{e}_{i\pm 1} \mathbf{e}_i = \mathbf{e}_i, \quad [\mathbf{e}_i, \mathbf{e}_j] = 0 \quad \text{for } |i - j| \geq 2, \quad (6)$$

where

$$\mathbf{e}_i = \begin{cases} D H_i^r & \text{for } i \text{ even,} \\ D H_i^p & \text{for } i \text{ odd.} \end{cases} \quad (7)$$

The characteristic ‘D-isotopy’ parameter of this Temperley-Lieb algebra, $D = \sqrt{1 + \varphi^2} = 2 \cos(\pi/10)$, is precisely the total quantum dimension of the underlying Fibonacci anyon liquid. We have thereby established a remarkable, explicit connection of the one parameter of this emerging algebraic structure, the ‘D-isotopy’ parameter of this Temperley-Lieb algebra, and the single most characteristic parameter of the underlying anyonic liquid, namely its total quantum dimension. This observation points to a generalization of such a connection for other quantum liquids. Written in this form, the resulting Hamiltonian for the Fibonacci anyon liquid turns out to be precisely that of the (integrable) restricted solid-on-solid (RSOS) statistical mechanics lattice model based on the D_6 -Dynkin diagram²⁴, as obtained in the standard fashion from the transfer matrix of the RSOS lattice model. For further details we refer to the supplementary material.

General framework. We have explicitly formulated the concept of a topology driven phase quantum phase transition mainly in the context of a single anyon theory, namely that of Fibonacci anyons. However, we note that these concepts apply in great generality to any anyon theory in which there can be an arbitrary number of anyons subject to a set of fusion rules / constraints.

Supplementary Material

I. FIBONACCI ANYONS

The degrees of freedom in our microscopic models are so-called Fibonacci anyons, one of the simplest types of non-abelian anyons^{14,34}. The Fibonacci theory has two distinct particles, the trivial state 1 and the Fibonacci anyon τ , which can be thought of as a generalization (or more precisely a ‘truncated version’) of an ‘angular momentum’ when viewing the Fibonacci theory as a certain deformation³⁵ of $SU(2)$. We will now make this notion more precise and illustrate it in detail. In analogy to the ordinary angular momentum coupling rules, we can write down a set of ‘fusion rules’ for the anyonic degrees of freedom which are analogs of the Clebsch-Gordon rules for coupling of ordinary angular momenta,

$$1 \times 1 = 1 \quad 1 \times \tau = \tau = \tau \times 1 \quad \tau \times \tau = 1 + \tau, \quad (8)$$

where the last fusion rule reveals what is known as the non-abelian character of the Fibonacci anyon: Two Fibonacci anyons τ can fuse to either the trivial particle or to another Fibonacci anyon. In more mathematical terms, these fusion rules can also be expressed by means of so-called fusion matrices N_j whose entries $(N_j)_{j_1 j_2}^{j_1}$ equal to one if and only if the fusion of anyons of types j_1 and j_2 into j is possible. The fusion rules are related to the so-called ‘quantum dimensions’ d_j of the anyonic particles by

$$N_j |d_j\rangle = d_j |d_j\rangle, \quad (9)$$

where $|d_j\rangle$ is the (‘Perron Frobenius’) eigenvector corresponding to the largest positive eigenvalue of the 2×2 -matrix N_j . [The sense in which these numbers are ‘dimensions’ will become apparent in section II A 1 below.] For the particles in the Fibonacci theory the quantum dimensions are $d_1 = 1$ and $d_\tau = \varphi \equiv (1 + \sqrt{5})/2$ and the total quantum dimension of the theory is then given by $D = (\sum_j d_j^2)^{1/2} = \sqrt{1 + \varphi^2}$.

To define our Hamiltonian, some additional ingredients of the theory of anyons are required. In analogy to the $6j$ -symbols for ordinary $SU(2)$ spins, there exists a basis transformation F that relates the two different ways three anyons can fuse to a fourth anyon, depicted as

$$\begin{array}{c} a & & b & & c \\ & \diagdown & & \diagup & \\ & e & & & \\ & & & & d \end{array} = \sum_f (F_{abc}^d)_e^f \begin{array}{c} a & & b & & c \\ & \diagdown & & \diagup & \\ & & & & f \\ & & & & d \end{array}. \quad (10)$$

The left hand side (l.h.s.) represents the quantum state that arises when anyon a first fuses with anyon b into an anyon of type e , which, subsequently, fuses with anyon c into an anyon of type d . Similarly, the right hand side (r.h.s.) denotes the quantum states that arises when anyon b first fuses with anyon c into anyon type f which, in turn, fuses with anyon a into anyon type d . Whilst keeping all external labels, the types of the three anyons (a, b, c) as well as the resulting anyon type d fixed, the states on the l.h.s and r.h.s. are fully specified by the labels e and f , respectively. Eq. (10) says the so-specified states are linearly related to each other by the so-called F -matrix³⁷ with matrix elements $(F_{abc}^d)_e^f$.

In general, the F -matrix is uniquely defined (up to ‘gauge transformations’) by the fusion rules through a consistency relation called the pentagon equation³⁶. Similarly, the braiding properties of anyons are given by the so-called R -matrix (which however is not needed here) that is uniquely determined by the hexagon equation³⁶.

For the Fibonacci theory, it is straightforward to verify that in most cases there is only one term on the right-hand-side in Eq. (10), e.g. by choosing two or three out of the four anyons a, b, c, d to be τ -anyons. For these cases the consistency with the pentagon and hexagon relations then yields that the corresponding F -matrix elements equal to 1. There is only one configuration that gives rise to F -matrix elements that are non-trivial: If all anyons are τ -anyons, e.g. $a = b = c = d = \tau$, both the 1- and the τ -fusion channels appear, and the F -matrix takes the explicit form

$$F_{\tau\tau\tau}^\tau = \begin{pmatrix} (F_{\tau\tau\tau}^\tau)_1^1 & (F_{\tau\tau\tau}^\tau)_\tau^\tau \\ (F_{\tau\tau\tau}^\tau)_1^\tau & (F_{\tau\tau\tau}^\tau)_\tau^1 \end{pmatrix} = \begin{pmatrix} \varphi^{-1} & \varphi^{-1/2} \\ \varphi^{-1/2} & -\varphi^{-1} \end{pmatrix}. \quad (11)$$

As a final ingredient to explicitly derive our Hamiltonian, we have to introduce the so-called modular S -matrix that relates the anyon ‘flux’ of species b through an anyon loop of species a to the case without anyon loop by

$$\begin{array}{c} |b \\ \bigcirc \\ |a \end{array} = \frac{S_a^b}{S_1^b} \begin{array}{c} |b \\ | \end{array}. \quad (12)$$

For the case of Fibonacci anyons, the S -matrix takes the explicit form

$$S = \begin{pmatrix} S_1^1 & S_\tau^1 \\ S_1^\tau & S_\tau^\tau \end{pmatrix} = \frac{1}{D} \begin{pmatrix} 1 & \varphi \\ \varphi & -1 \end{pmatrix}. \quad (13)$$

There is an important relationship between the modular S -matrix and the matrix encoding the fusion rules, introduced in the paragraph above Eq. (9): the modular S -matrix *diagonalizes* the fusion rules, the ‘Verlinde Formula’,

$$S_{b'}^b (N_a)_{c'}^{b'} S_c^\dagger = \delta_c^b \frac{S_b^a}{S_1^1}, \quad (14)$$

(repeated indices are summed) where S^\dagger denotes the adjoint of the unitary matrix S . The eigenvalues of the matrix (N_a) are thus $\frac{S_b^a}{S_1^1}$, and the largest (positive) eigenvalue, the quantum dimension d_a , can be seen to be

$$d_a = \frac{S_1^a}{S_1^1}. \quad (15)$$

Due to the unitarity of the modular S -matrix one immediately checks that the total quantum dimension equals

$$D = \frac{1}{S_1^1}. \quad (16)$$

II. THE LADDER MODEL

In this section we will discuss details of the ‘ladder model’ in a one-dimensional geometry, whose Hamiltonian is given by Eq. (2) in the main part of the paper. We start by defining the Hamiltonian in detail, and then discuss the gapped topological phases, critical phases, and the exact solutions.

A. The Hamiltonian

1. Explicit expression

To establish a notation for the basis states we consider the skeleton lattice inside the high-genus ladder geometry as shown in Fig. 7. The basis states are given by all admissible labeling of the edges of the skeleton with 1 or τ particles, subject to the vertex constraints given by the fusion rules. The number of basis states, B_L , of the ladder with L plaquettes and periodic boundary conditions is given by

$$B_L = \sum_{\{a_i, b_i, c_i\}} (N_{c_1})_{a_1}^{a_2} (N_{c_2})_{a_2}^{a_3} \dots (N_{c_L})_{a_L}^{a_1} (N_{c_1})_{b_1}^{b_2} (N_{c_2})_{b_2}^{b_3} \dots (N_{c_L})_{b_L}^{b_1} = \sum_{\{i_1, \dots, i_L\}} [\text{Tr}(N_{i_1} N_{i_2} \dots N_{i_L})]^2, \quad (17)$$

where N_i are the fusion matrices of Fibonacci theory as introduced above. The largest eigenvalue of the matrix N_i is the quantum dimension d_i . Thus, the leading behavior of the traces for large L is,

$$B_L \sim \sum_{\{i_1, \dots, i_L\}} (d_{i_1} d_{i_2} \dots d_{i_L})^2 = \sum_{k=0}^L (d_1^2)^{L-k} (d_\tau^2)^k = (1 + \varphi^2)^L = D^{2L}. \quad (18)$$

The Hilbert space thus grows asymptotically, for large L , as a power of the square of the total quantum dimension D^2 .

The Hamiltonian (as given in Eq. (2) of the main part of the paper)

$$H = -J_r \sum_{\text{rungs } r} \delta_{\ell(r), 1} - J_p \sum_{\text{plaq } p} \delta_{\phi(p), 1} \quad (19)$$

consists of two non-commuting terms, the rung term which is diagonal in the chosen basis, and the plaquette term which depends on the four edges of the plaquette p , and the four adjoining edges. By inserting an additional anyon loop of type s into the center of the plaquette, we can project onto the flux through this additional loop (and hence the flux through the plaquette) by the following procedure (for a derivation see the following subsection)

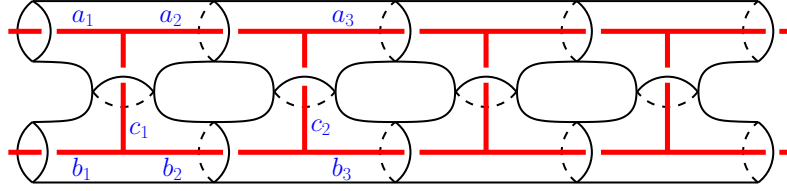


FIG. 7: The high-genus surface in a ladder geometry and the ‘skeleton’ of the fusion graph that defines the Hilbert space. The trivial particle 1 or the Fibonacci anyon τ can occupy the links of the ladder skeleton, subject to the vertex constraints given by the fusion rules of Fibonacci anyons.

$$\delta_{\phi(p),1} \left| \begin{array}{c|c|c} a & \alpha & b \\ \delta & & \beta \\ \hline d & \gamma & c \end{array} \right\rangle = \sum_{s=1,\tau} \frac{d_s}{D^2} \left| \begin{array}{c|c|c} a & \alpha & b \\ \delta & s & \beta \\ \hline d & \gamma & c \end{array} \right\rangle. \quad (20)$$

The additional s -loop is inserted by performing a sequence of F -transformations:

$$\begin{aligned} \left| \begin{array}{c|c|c} a & \alpha & b \\ \delta & s & \beta \\ \hline d & \gamma & c \end{array} \right\rangle &= \sum_{\delta'} (F_{\delta\delta s}^s)^{\delta'} \left| \begin{array}{c|c|c} a & \alpha & b \\ \delta & \delta' & \beta \\ \hline d & \gamma & c \end{array} \right\rangle = \sum_{\delta',\gamma'} (F_{\delta\delta s}^s)^{\delta'} (F_{d\delta's}^\gamma)^{\gamma'} \left| \begin{array}{c|c|c} a & \alpha & b \\ \delta & \delta' & s \\ \hline d & \gamma' & \gamma & c \end{array} \right\rangle \\ &= \sum_{\delta',\gamma',\beta'} (F_{\delta\delta s}^s)^{\delta'} (F_{d\delta's}^\gamma)^{\gamma'} (F_{c\gamma's}^\beta)^{\beta'} \left| \begin{array}{c|c|c} a & \alpha & b \\ \delta & s & \beta \\ \hline d & \gamma' & c \end{array} \right\rangle = \sum_{\delta',\gamma',\beta',\alpha'} (F_{\delta\delta s}^s)^{\delta'} (F_{d\delta's}^\gamma)^{\gamma'} (F_{c\gamma's}^\beta)^{\beta'} (F_{b\beta's}^\alpha)^{\alpha'} \left| \begin{array}{c|c|c} a & \alpha & \alpha' & b \\ \delta & \delta' & s & \beta' \\ \hline d & \gamma' & c \end{array} \right\rangle \\ &= \sum_{\delta',\gamma',\beta',\alpha',m} (F_{\delta\delta s}^s)^{\delta'} (F_{d\delta's}^\gamma)^{\gamma'} (F_{c\gamma's}^\beta)^{\beta'} (F_{b\beta's}^\alpha)^{\alpha'} (F_{a\alpha's}^\delta)^m \left| \begin{array}{c|c|c} a & \alpha' & b \\ \delta & \delta' & s \\ \hline d & \gamma' & c \end{array} \right\rangle. \end{aligned} \quad (21)$$

Using the identities

$$\delta \begin{array}{c} m \\ \bigcirc \\ \delta' \end{array} s = \delta_{m\delta'} (F_{\delta\delta s}^s)^{\delta'} \left| \delta' \right\rangle, \quad (22)$$

and $(F_{abc}^d)^f_e = (F_{bcd}^a)^e_f$, we obtain the final expression

$$\delta_{\phi(p),1} \left| \begin{array}{c|c|c} a & \alpha & b \\ \delta & & \beta \\ \hline d & \gamma & c \end{array} \right\rangle = \sum_{s=1,\tau} \frac{d_s}{D^2} \sum_{\alpha',\beta',\gamma',\delta'} (F_{d\delta's}^\gamma)^{\gamma'} (F_{c\gamma's}^\beta)^{\beta'} (F_{b\beta's}^\alpha)^{\alpha'} (F_{a\alpha's}^\delta)^{\delta'} \left| \begin{array}{c|c|c} a & \alpha' & b \\ \delta' & & \beta' \\ \hline d & \gamma' & c \end{array} \right\rangle. \quad (23)$$

The ladder geometry has a local duality between the inside and outside: the inside of the rungs is dual to the plaquettes. The only difference is that the rungs connect two different cylinders, while the plaquettes connect the same space (the ‘outside’). The duality can be made exact by using ‘twisted’ boundary conditions where the ends of the ladder are connected according to $a_1 = b_{L+1}$ and $b_1 = a_{L+1}$ (so that the ladder looks like a Moebius strip). Indeed, our exact diagonalization results confirm that the excitation spectra are identical under exchange of the couplings J_r and J_p for twisted boundary conditions. However, in the case of periodic boundary conditions ($a_1 = a_{L+1}$, $b_1 = b_{L+1}$), which we shall focus on in the following, this duality is only up to degeneracies.

2. Bigger (mathematical) picture

So far our discussion in this ‘Supplementary Material’ has been largely focused on detailed algebraic manipulations. In this subsection we wish to give a brief idea of the general bigger picture of topological field theories which underlies these detailed manipulations. At the same time we will provide a deeper understanding of the so-called ‘Levin-Wen model’ within this context.

In the main text we have given a physically motivated description of the Levin-Wen model in Figs. 1 and 2, leading to the Hamiltonian in Eq. (1) of the main text. Let us now give a more abstract description of it. The most general Levin-Wen Hamiltonian has two kinds of terms: the vertex type (not discussed so-far as a term of the Hamiltonian) and plaquette type. Let us consider a surface Σ , and a trivalent graph Γ (which we called ‘skeleton’ in the main text) embedded in that surface. (The sole role of the surface Σ , which in the leftmost picture of Fig. 1 of the main text is just a parallel plane sitting in between the two depicted sheets, is to give a well defined meaning to the notion of a ‘plaquette’; namely, all complimentary regions of $\Sigma \setminus \Gamma$, i.e. the complimentary regions of the graph Γ within the surface Σ , are plaquettes.) We always enforce strictly the condition that three labels meeting at a vertex must satisfy the fusion rule. (This is another way of saying that we have set the coupling constant of the ‘vertex term’ in the most general Levin-Wen Hamiltonian to infinity.) As a result, we obtain a Hilbert space called $L(\Gamma, \Sigma)$ consisting of the Hilbert space spanned by all admissible labelings of the trivalent graph Γ : a labeling of Γ is an assignment of a label in a label set $I_{\mathcal{C}}$ to each edge of the graph, [$I_{\mathcal{C}} = \{\mathbf{1}, \tau\}$ in the previous subsection I], and the labeling is admissible if the three labels around each vertex satisfy the fusion rules.

Now, there exists another vector space, which brings about the connection with the actual surfaces that were drawn in Figs. 1 and 2 of the main text. In particular, when \mathcal{C} denotes a so-called modular category (for a precise definition, which we do not need at the moment, see e.g. Ref. 41) which basically denotes a theory of ‘anyons’ and their corresponding ‘fusion rules’ such as the one described in the previous subsection I, then the vector space $L(\Gamma, \Sigma)$ is the same as a Hilbert space $V_{\mathcal{C}}(S_{\Gamma})$ (for a definition see e.g. Ref. 41) of an associated Topological Quantum Field Theory (TQFT) corresponding to the ‘modular category’ \mathcal{C} : specifically let N_{Γ} be the thickening of the graph Γ to a handle-body (drawing a cylinder around each edge of the graph), and S_{Γ} be the boundary surface of N_{Γ} , then $L(\Gamma, \Sigma) \cong V_{\mathcal{C}}(S_{\Gamma})$. In the language of TQFT, any ‘pants-decomposition’ of the surface S_{Γ} is known to lead to a basis of $V_{\mathcal{C}}(S_{\Gamma})$, which corresponds to the vector space spanned all possible fusions of the labelings on Γ .

This interpretation of the Hilbert space $L(\Gamma, \Sigma)$ gives rise to a transparent derivation of the plaquette term, Eq. (23), in the Levin-Wen model. To derive this expression, we use the identification of $L(\Gamma, \Sigma)$ with $V_{\mathcal{C}}(S_{\Gamma})$. The c th row of the modular S -matrix of the modular category \mathcal{C} can be used to construct a projector ω_c that projects out the particle with a label c through a plaquette. In other words total flux c through a plaquette p can be enforced by inserting ω_c into a plaquette p . The projector turns out to be of the form

$$\omega_c = \frac{1}{D} \sum_a S_c^a [a], \quad (24)$$

where $[a]$ denotes a loop labeled by a as the one drawn in Eq. (12). In order to see that this performs the task let us insert a flux with label b through the loop $[a]$, resulting in the figure drawn on the l.h.s. of Eq. (12), which we denote in symbols by $[a](b)$. When we now perform the sum in Eq. (24) we obtain, upon making use of Eq. (12),

$$\omega_c(b) := \frac{1}{D} \sum_a S_c^a [a](b) = \frac{1}{D} \sum_a S_c^a \frac{S_a^b}{S_1^b} [b] = \delta_c^b \frac{1}{D S_1^c} [c] = \delta_c^b \frac{1}{d_c} [c] \quad (25)$$

$$\omega_c \left(\left(\begin{array}{c} b \\ | \\ | \\ | \\ | \end{array} \right) \right) := \frac{1}{D} \sum_a S_c^a \left(\begin{array}{c} b \\ | \\ \bigcirc \\ | \\ a \end{array} \right) = \delta_c^b \frac{1}{d_c} \left(\begin{array}{c} | \\ | \\ | \\ | \end{array} \right) \quad (26)$$

where we have used the unitarity (plus reality and symmetry) of the modular S -matrix, as well as Eq.s (15,16).

Therefore, the plaquette term $\delta_{\phi(p),1}$ is implemented by inserting the projector $\omega_1 = \sum_a \frac{d_a}{D^2} [a]$ into the plaquette p . Now the detailed steps leading to Eq. (23) are easy to understand: The insertion of ω_1 into the plaquette is written explicitly in Eq. (20). In the subsequent equation, first an F -move is applied to the two lines connected by the dotted line, and subsequently four more F moves counterclockwise around p are implemented as drawn; finally removing the resulting bubble, we obtain the explicit form of the plaquette term written in Eq. (23).

The mathematical context for the Levin-Wen model is the Drinfeld center $Z(\mathcal{C})$ or quantum double of a unitary fusion category \mathcal{C} . The label set $I_{\mathcal{C}}$ for the Levin-Wen Hamiltonian is the isomorphism classes of simple objects of \mathcal{C} . It is known that a unitary fusion category is always spherical. By a theorem of M. Müger³⁹, the Drinfeld center of any spherical category is always modular. It follows that the Drinfeld center of any unitary fusion category is always modular. Moreover, if the spherical category \mathcal{C} itself is modular, then $Z(\mathcal{C})$ is isomorphic to the direct product of the conjugate \mathcal{C}^* and \mathcal{C} , where \mathcal{C}^* is obtained from \mathcal{C} by complex conjugating all data. Our main example is one of those special cases, where \mathcal{C} is the Fibonacci theory.



FIG. 8: Possible basis configurations in the presence of one plaquette excitation. The two ground states (without a flux through the plaquette) and three excited states (with a τ -flux through the plaquette) are linear combinations of these basis states. Solid lines denote τ -anyons while dashed lines symbolize the trivial particle 1.

The decomposition of $Z(\mathcal{C})$ hints directly at the appearance of Dynkin diagram D_6 at the critical point in one-dimensional geometry: indeed, the two phases connected by the critical point are the Fibonacci theory and the doubled Fibonacci theory with label sets $\{1, \tau\}$, and $\{(1, 1), (1, \tau), (\tau, 1), (\tau, \tau)\}$, respectively. Based on this, it is natural to expect that the two sets of fusion rules will fit together in a compatible way at the critical point, which is nicely illustrated by the structure of the D_6 Dynkin diagram in Fig. 17 which underlies the exact solution of this critical point (Section II D below).

B. Topological phases

We start the detailed discussion of the phase diagram with the two distinct gapped non-abelian topological phases: the ‘single torus’ phase where all plaquettes are closed at $\theta = 0$ and the ‘two tori’ phase with closed off rungs at $\theta = \pi/2$. A finite-size scaling analysis of the splitting of the ground state degeneracies and the energy gap shows that the phases extend over a wide range of parameter space as illustrated in the phase diagram (Fig. 5b of the main part of the paper). In this section we discuss the low-lying excited states in these phases, give their explicit wave functions at the exactly solvable points, and a perturbative expansion for their dispersion away from these points.

1. The ‘single torus’ phase at $-\pi/2 < \theta < \pi/4$

To describe the lowest excited states we consider the trivially solvable point $\theta = 0$ where $J_r = 0$. In the ground state there is no flux through any of the plaquettes, and they all can be closed, thus reducing the high-genus ladder to a single torus (see Fig. 3 in the main part of the paper). There are two degenerate ground-states configurations with either no flux or a τ -flux through this torus.

Similarly, we can deduce the degree of degeneracy for the lowest excited state by considering the topology of this state. In the lowest excited state, one plaquette flux is present which yields the reduced topology (as compared to the high-genus ladder) and the associated skeleton shown in Fig. 4b of the main part of the paper. Closing all but one plaquette this skeleton allows for 5 different $1, \tau$ coverings, illustrated schematically in Fig. 8. In order to obtain the anyon-fluxes through the excited plaquette, a basis transformation (consisting of a F - and a S -transformation) of the reduced basis is performed which yields that there are three τ -fluxes through each plaquette. Thus, the lowest excited state at $\theta = 0$ is $3L$ -fold degenerate. Tuning away from $\theta = 0$ these $3L$ excitations delocalize and form a three-fold degenerate band.

2. The ‘two tori’ phase at $\pi/4 < \theta < \pi$

At the point $\theta = \pi/2$ (trivially solvable) the ground state has no τ -anyons on the rungs of the ladder. The rungs can hence be cut which yields an effective topology of two separate tori. Of the four degenerate ground states three are symmetric and one is antisymmetric under y -reflection. The lowest excited state is a τ -anyon flux through a single rung. The fusion rules then require a flux through both of the two tori, and this state is hence only L -fold degenerate. Tuning away from $\theta = \pi/2$, these states delocalize into a non-degenerate band.

3. Perturbation expansion for the quasiparticle bands

Over a broad range of parameters the quasi-particle excitations are well described (see Fig. 5b of the main part of the paper) by a second order perturbative expansion around $\theta = \pi/2$, with a dispersion given by

$$\Delta E(J_p, J_r, k_x) = J_r - \frac{2J_p}{D^2} \cos(k_x) - \frac{J_p^2 \varphi}{D^4 J_r} [1 + 2 \cos(k_x)] - \frac{J_p^2}{2D^4 J_r} 2 \cos(2k_x). \quad (27)$$

Due to duality, this result equally applies for coupling parameters θ close to $\theta = 0$, with J_r and J_p interchanged.

C. Gapless theories

In this section, we discuss the critical points ($\theta = \pi/4, 5\pi/4$) and the extended critical phase in the ladder model. We first discuss the gapless theories in terms of numerical results and then present analytical arguments leading to an exact solution for the two critical points ($\theta = \pi/4, 5\pi/4$).

1. Critical point at $\theta = \pi/4$ (numerical findings from exact diagonalization)

At equal positive values of the two coupling constants ($J_p = J_r, \theta = \pi/4$), the system has a linear energy-momentum dispersion relation with the finite-size spacing between energy levels vanishing linearly in $1/L$. This indicates that the two adjacent, gapped topological phases (Fig. 5) are separated by a continuous quantum phase transition and a critical point that is described by a 2D conformal field theory (CFT). To characterize this CFT, we rescale and match the finite-size energy spectra obtained numerically by exact diagonalization for systems with up to $L = 36$ anyons to the form of the spectrum of a CFT,

$$E = E_1 L + \frac{2\pi v}{L} \left(-\frac{c}{12} + h + \bar{h} \right), \quad (28)$$

where the velocity v is an overall scale factor, and c is the central charge of the CFT. The scaling dimensions $h + \bar{h}$ take the form $h = h^0 + n, \bar{h} = \bar{h}^0 + \bar{n}$, with n and \bar{n} non-negative integers, and h^0 and \bar{h}^0 are the holomorphic and antiholomorphic conformal weights of primary fields in a given CFT with central charge c . The momenta (in units $2\pi/L$) are such that $k_x = h - \bar{h}$ or $k_x = h - \bar{h} + L/2$. Using this procedure, we find that for the critical point at $\theta = \pi/4$ the rescaled energy spectrum matches the assignments (28) of part of the Kac-Table of the $m = 9$ unitary Virasoro minimal CFT of central charge $c = 14/15$, as shown in Fig. 9. In Fig. 10 we list all relevant primary fields of this CFT which appear and their corresponding scaling dimensions. It turns out that only the Kac-Table primary fields $\phi_{r,s}$ with $s = \text{odd}$ appear, and those with $s = 5$ have multiplicity two (the associated states on the ladder being in the bonding/antibonding sectors of ‘transverse momenta’ $k_y = 0, \pi$), all others having multiplicity one. These are precisely those Kac-table primary fields which occur in the so-called (D,A)-modular invariant⁴⁰ of the $m = 9$ th Virasoro minimal CFT of central charge $c = 14/15$.

To illustrate how the ground-state degeneracy changes at this critical point from a two-fold degeneracy for the ‘single cylinder’ limit ($J_r = 0$) to a four-fold degeneracy for the ‘two cylinders’-limit ($J_p = 0$), we can follow the evolution of eigenenergies

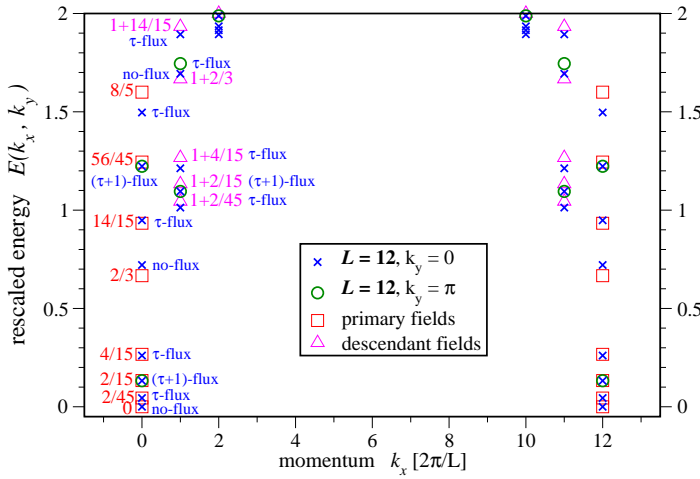


FIG. 9: Exact diagonalization: Energy spectrum at the critical point ($\theta = \pi/4$) for a ladder with $L = 12$ holes and 36 anyons. The energies have been rescaled so that the two lowest eigenvalues match the CFT scaling dimensions. The open boxes indicate the primary fields of the 7th minimal model with central charge $c = 14/15$. The topological symmetry sectors are indicated with symbols $1 \equiv y_{1,1}$, $\tau \equiv y_{\tau,\tau}$ and $\tau + 1 \equiv y_{1,\tau}$.

(r, s)	$h_{(r,s)} + \bar{h}_{(r,s)}$	k_x	k_y	y
(1, 1)	0	0	0	φ^{-2}
(3, 3)	$\frac{2}{45}$	0	0	φ^{-2}
(5, 5)	$\frac{2}{15}$	0	0	-1
(5, 5)	$\frac{2}{15}$	0	π	-1
(7, 7)	$\frac{4}{15}$	0	0	φ^{-2}
(2, 1)	$\frac{2}{3}$	0	0	φ^{-2}
(4, 3)	$\frac{14}{15}$	0	0	φ^{-2}
(6, 5)	$\frac{56}{45}$	0	0	-1
(6, 5)	$\frac{56}{45}$	0	π	-1
(8, 7)	$\frac{8}{5}$	0	0	φ^{-2}

FIG. 10: CFT fields: Scaling dimensions $h_{(r,s)} + \bar{h}_{(r,s)}$ of the primary fields in the (D, A) modular invariant of the 7th minimal model with central charge $c = 14/15$. On the right, we give momentum and topological symmetry assignments of these primary fields for our microscopic model.

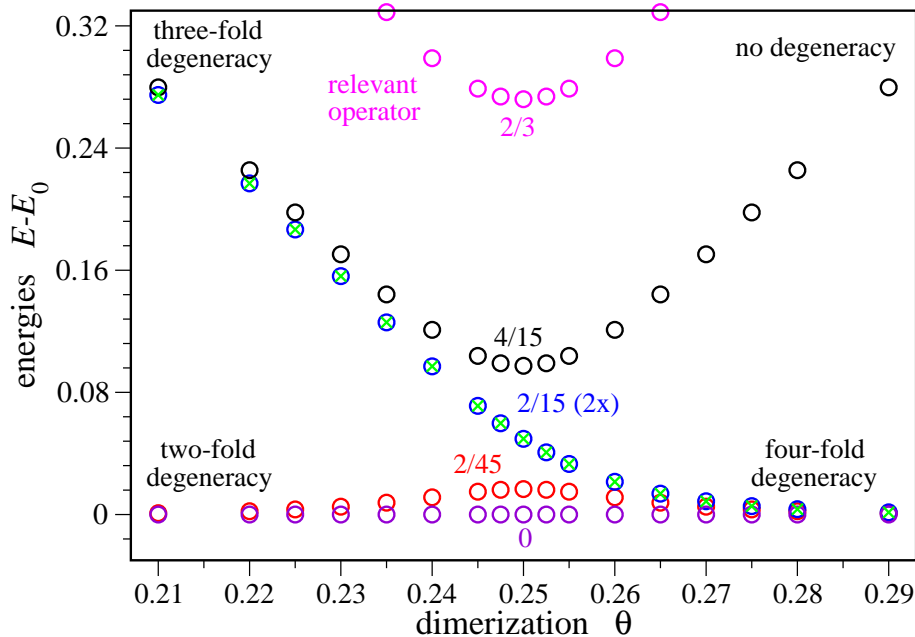


FIG. 11: The energies of the lowest lying energy states around the critical point ($\theta = \pi/4$) as a function of the ‘dimerization’ θ . Results are shown for system size $L = 10$.

in the vicinity of this critical point as shown in Fig. 11. Moving away from the critical point ($\theta = \pi/4$) corresponds to a dimerization of the model: in an alternative basis choice, discussed in detail in section IID, it becomes apparent that the rung and plaquette terms alternately act on even and odd ‘sites’. For $\theta \searrow \pi/4$, the four-fold ground-state degeneracy is lifted with one of the four ground states approaching the field with rescaled energy $2/45$ ($k_y = 0$), and two degenerate ground states moving to a rescaled energy $2/15$ ($k_y = 0$ and $k_y = \pi$). The single first excited state in this gapped phase softens towards the rescaled energy $4/15$ at the critical point. As we move into the adjacent gapped phase for $\theta < \pi/4$ only the field with rescaled eigenenergy $2/45$ moves back towards the ground-state, while the two other fields move upwards in energy and form a three-fold degenerate excited state.

2. *Extended critical phase for $\theta \in (\pi, 3\pi, 2)$
(numerical findings from exact diagonalization)*

For negative coupling parameters $J_p, J_r < 0$, we find an extended critical phase around the point of equal coupling strength which in our circle phase diagram is opposite to the critical point discussed above. For the whole extent of this critical phase we can match the finite-size energy spectra to the Z_8 parafermion CFT with central charge $c = 7/5$. This theory is part of the sequence of Z_k -parafermion CFTs with conformal weights $\Delta_m^j = \frac{j(j+1)}{k+2} - \frac{m^2}{k}$, where $j = 0, \frac{1}{2}, 1, \dots, k/2$, $|m| \leq j$ (and $j - m = \text{integer}$), in the notation of⁴². The details of the assignments for $k = 8$ can be found in Fig. 12 and Table II.

In order to verify that the critical phase around the exactly soluble point $\theta = 5\pi/4$ extends to the vicinity of the decoupling points $\theta = \pi$ and $\theta = 3\pi/2$, we consider an effective model where we fix all rung occupations to τ -anyons. This assumption is exactly true at the decoupling point $\theta = 3\pi/2$. Implementing this constraint significantly reduces the size of the Hilbert space and allows us to numerically study this effective model for larger system sizes with up to 48 anyons.

The effective Hamiltonian in the reduced Hilbert space is given by

$$H^{\text{eff}} = -LJ_r - J_p \sum_{\text{plaq } p} \delta_{\phi(p),1}. \quad (29)$$

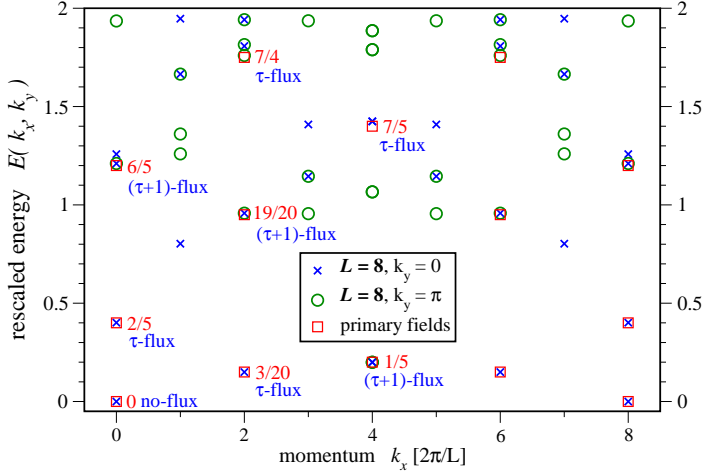


FIG. 12: Exact diagonalization: Energy spectrum at the critical point ($\theta = 5\pi/4$) for a ladder with $L = 8$ holes and 24 anyons. The energies have been rescaled so that the two lowest eigenvalues match the CFT scaling dimensions. The open boxes indicate the primary fields of the Z_8 -parafermion model with central charge $c = 7/5$. The topological symmetry sectors are indicated with symbols $1 \equiv y_{1,1}$, $\tau \equiv y_{\tau,\tau}$ and $\tau + 1 \equiv y_{1,\tau}$.

(j, m)	$h_{(j,m)} + \bar{h}_{(j,m)}$	k_x	k_y	y
(0, 0)	0	0	0	φ^2
(1, 1)	$\frac{3}{20}$	$\frac{\pi}{4}$	0	φ^{-2}
(2, 2)	$\frac{1}{5}$	$\frac{\pi}{2}$	0	-1
(2, 2)	$\frac{1}{5}$	$\frac{\pi}{2}$	π	-1
(1, 0)	$\frac{2}{5}$	0	π	φ^{-2}
(2, 1)	$\frac{19}{20}$	$\frac{\pi}{4}$	0	-1
(2, 1)	$\frac{19}{20}$	$\frac{\pi}{4}$	π	-1
(2, 0)	$\frac{6}{5}$	0	0	-1
(2, 0)	$\frac{6}{5}$	0	π	-1
(3, 2)	$\frac{7}{5}$	$\frac{\pi}{2}$	0	φ^{-2}
(4, 3)	$\frac{7}{4}$	$\frac{\pi}{4}$	0	φ^{-2}

FIG. 13: CFT fields: Scaling dimensions $h_{(j,m)} + \bar{h}_{(j,m)}$ of the primary fields in the Z_8 -parafermion CFT with central charge $c = 7/5$. On the right, we give momentum and topological symmetry assignments of these primary fields for our microscopic model.

The first term is a constant, and can thus be omitted which then turns the actual value of J_p irrelevant. A positive J_p corresponds to the limit $\theta \searrow 3\pi/2$, while a negative J_p allows to study the limit $\theta \nearrow 3\pi/2$.

For positive J_p , we find that the splitting of the ground state degeneracies goes to zero for $1/L \rightarrow 0$, and the energy gap approaches a finite value as shown in Fig. 14. This further supports the stability of the gapped topological phases up to, but excluding, the points $\theta = \pi$ and $\theta = 3\pi/2$ in our phase diagram.

For negative J_p , the rescaled energy spectrum of this effective model is critical and again matches (with much higher accuracy than at $\theta = \pi$) the Z_8 parafermion conformal field theory with central charge $c = 7/5$ as shown in Fig. 12. We can hence conclude that the whole quadrant $\theta \in (\pi, 3\pi/2)$ is occupied by an extended critical phase described by the same conformal field theory as the exactly solvable point $\theta = 5\pi/4$.

Approaching the endpoints of this extended critical phase at $\theta = \pi$ and $\theta = 3\pi/2$, the low-energy spectrum collapses into a flat band resulting in an extensive ground state degeneracy below an energy gap of size 1 at the points $\theta = \pi$ and $\theta = 3\pi/2$. Moving beyond these ‘decoupling points’ where one of the terms in the Hamiltonian vanishes, this extensive ground-state degeneracy is split again and a gap opens for $\theta < \pi$ and $\theta > 3\pi/2$, respectively, as the system enters the two gapped, topological phases discussed above.

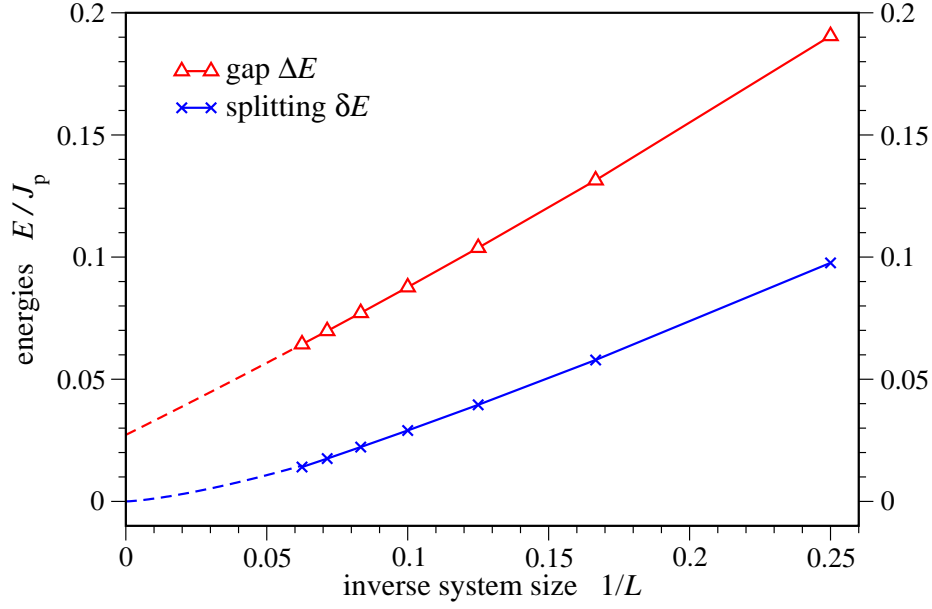


FIG. 14: Energy gap $\Delta E(1/L)/J_p$ between the first excited state and the ground state, as well as the splitting of the ground state degeneracy, $\delta E(1/L)/J_p$, for the effective model Eq. 29. The two ground states become precisely degenerate only in the thermodynamic limit. The results indicate that the energy gap extrapolates to a finite value. Since the effective model is valid in the limit $\theta \rightarrow 3\pi/2+$, the gapped topological phase extends all the way up to this point.

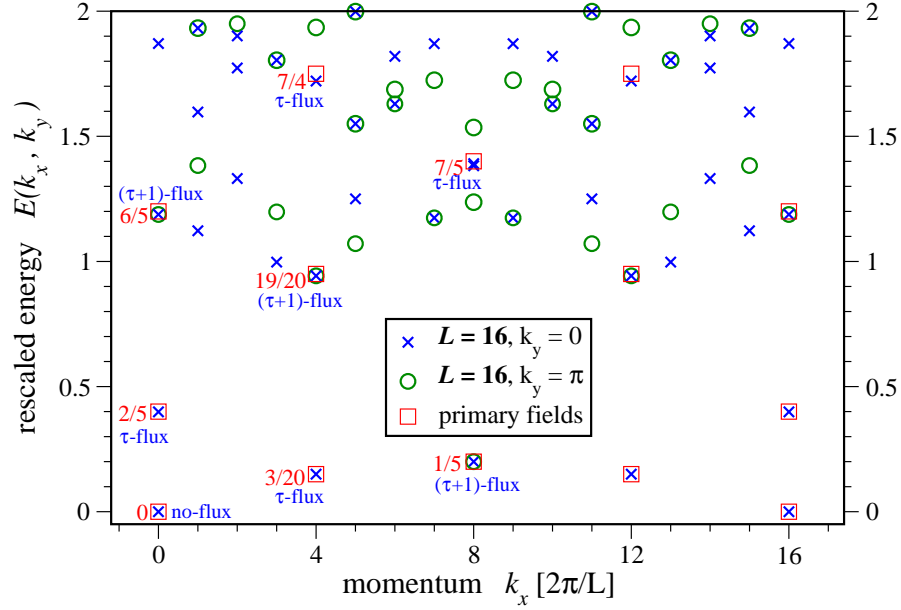


FIG. 15: Rescaled energy spectrum of the effective model with J_p negative ($L = 16$), and Z_8 parafermion CFT assignments. The topological symmetry sectors are indicated with symbols 1 ($y_{1,1} = \varphi^2$), τ ($y_{\tau,\tau} = \varphi^{-2}$) and $\tau + 1$ ($y_{1,\tau} = -1$).

3. Topological stability of the critical phases

Both critical theories have a large number of rescaled energies (28) that are smaller than two. These eigenenergies are associated with operators whose correlation functions decay with scaling exponent $h + \bar{h} < 2$. Such operators are relevant in the renormalization group sense. This means that any operators \mathcal{O} with scaling dimensions (=rescaled energies) $h + \bar{h} < 2$ which is invariant under all symmetries of the Hamiltonian may appear as an additional term in the latter and can thus drive the system out of the critical phase into a gapped phase or a different critical phase. For a critical phase to be stable there must hence exist a symmetry in the model such that the identity field (associated with the ground state) belongs to a different symmetry sector than all other fields ϕ with $h + \bar{h} < 2$ and $k_x = 0$ (fields at $k_x \neq 0$ do not obey the translational symmetry of the Hamiltonian). Indeed, our model has an additional topological symmetry²⁶ that can stabilize the critical phases: There can be either no flux (denoted as 1-flux) or a τ -flux entering the periodic ladder from one side, and a 1- or a τ -flux leaving the ladder as illustrated in Fig. 16. There are hence three possibilities for possible flux assignments: (i) no flux is entering from above, and no flux is leaving [Fig. 16a], (ii) a τ -flux is entering and leaving [Fig. 16b], or, (iii) a τ -flux is entering from one side, and leaves through one or several plaquettes as shown in Fig. 16c). For each operator, one of the three scenarios applies and we can explicitly determine the topological sectors by considering the following hermitian symmetry operator (which commutes with the Hamiltonian)

$$Y|a, b, c\rangle = \sum_{a', b'} \prod_{i=1}^L (F_{c_i a_i \tau}^{a'_{i+1}})_{a'_i}^{a_{i+1}} (F_{c_i b_i \tau}^{b'_{i+1}})_{b'_i}^{b_{i+1}} |a', b', c\rangle, \quad (30)$$

where $|a, b, c\rangle = |a_1, b_1, c_1, a_2, b_2, c_2, \dots, a_L, b_L, c_L\rangle$ are labels according to Fig. 7. This operator inserts additional τ -loops parallel to the two ‘spines’ of the ladder. As in the case of the plaquette term Eq. (23), this is done by connecting them to the ladder with 1-particles. The flux through each of these two additional τ -loops can be either 1 or τ , where a 1-flux yields a factor of $S_1^\tau/S_1^1 = \varphi$, and a τ -flux gives $S_\tau^\tau/S_\tau^1 = -\varphi^{-1}$ (note that a S -transformation has to be performed in order to obtain the flux through the additional τ -loops). Hence there are three possible eigenvalues of Y : $y_{1,1} = \varphi^2$ (scenario i), $y_{\tau,\tau} = \varphi^{-2}$ (scenario ii) or $y_{1,\tau} = -\varphi^{-1}\varphi = -1$ (scenario iii).

We numerically evaluate the topological symmetry sectors in the two critical phases (see Tables I and II, and Figs. 9, 12 and 15). At the critical point separating the topological phases ($\theta = \pi/4$), we find that the relevant operators can be classified according to $s = 1 \leftrightarrow y_{1,1}$, $s = 3, 7 \leftrightarrow y_{\tau,\tau}$, $s = 5 \leftrightarrow y_{1,\tau}$. In particular, only one operator, $\phi_{(2,1)}$, is in the same topological symmetry sector as the ground state, i.e. the identity field $\phi_{(1,1)}$. It is this field that drives the system out of the critical phase when varying the coupling constant θ . With the scaling dimension of this operator being $x = 2/3$ the gap opens as $\Delta E(\theta) \propto |\theta - \pi/4|^\nu$ on either side of the critical point, where $\nu = 1/(2 - 2/3) = 3/4$. In the second critical phase, $\theta \in (\pi, 3\pi/2)$, the topological symmetry assignments of the relevant operators are given by $r = 0 \leftrightarrow y_{1,1}$, $r = 2, 6 \leftrightarrow y_{\tau,\tau}$, $r = 4 \leftrightarrow y_{1,\tau}$. In particular, there is no relevant field in the same topological symmetry sector as the ground state, which implies that there is no symmetry-allowed relevant operator in this gapless theory and the critical point must be part of an extended gapless phase. This observation demonstrates that our observation (from exact diagonalization studies) that the extended critical phase in the quadrant $\theta \in (\pi, 3\pi/2)$ is described by the same Z_8 parafermion CFT with central charge $c = 7/5$ is correct.

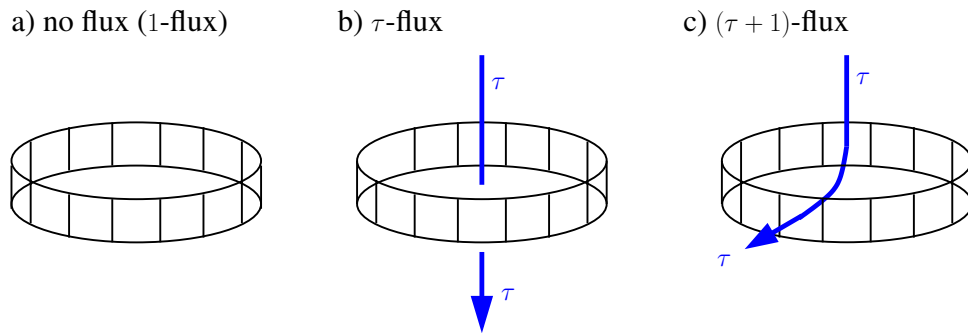


FIG. 16: Topological symmetry sectors: a) No τ -flux enters or leaves the ladder. b) A τ -flux enters from one side and leaves at the other side. c) A τ -flux enters from one side and leaves through a plaquette.

D. Analytical solution

Our ladder model defined by the Hamiltonian in Eq. (2) in the main part of the paper can be *solved exactly* at the two critical points $\theta = \pi/4$ and $\theta = 5\pi/4$ (see the phase diagram in Fig. 5 of the main text). The key observation leading to this exact solution is that the topological structure of our model implies that its Hilbert space is in fact built on the so-called D_6 -Dynkin diagram, which is drawn below in Fig. 17.

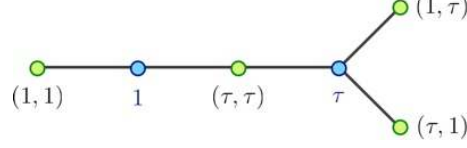


FIG. 17: Dynkin diagram D_6 .

The Dynkin diagram indeed appears very naturally: let us make a change of basis for our Hamiltonian as illustrated in Fig. 18. This new choice of basis (drawn on the left), which arises from a different decomposition of the high-genus surface, is related to the original one (drawn on the right) by a simple F -transformation. In particular, consider the new basis in the left part of Fig. 18: with the even-numbered ‘sites’ (which correspond to the original rungs) we associate a label $d_i = 1$ or $d_i = \tau$ (the flux through that cross-section of the surface). With the odd-numbered ‘sites’ (which correspond to the original plaquettes) we associate a variable consisting of a pair of labels, (a_i, b_i) which can assume four values, i.e., $(a_i, b_i) = (1, 1)$, $(a_i, b_i) = (\tau, 1)$, $(a_i, b_i) = (1, \tau)$ and $(a_i, b_i) = (\tau, \tau)$, and denotes the pair of fluxes through the two cross-sections of the surface at the position of the plaquette. The allowed fusion channels at the vertices where variables (a_i, b_i) and $d_{i\pm 1}$ meet then correspond precisely to the condition that they be adjacent nodes on the Dynkin diagram of the D_6 Lie algebra, as illustrated in Fig. 17 above. For example, a local label $(a_i, b_i) = (\tau, \tau)$ at an odd-numbered ‘site’ i allows for labels $d_{i-1} = 1$ and $d_{i+1} = \tau$ at the neighboring even-numbered sites, which is reflected in the fact that label (τ, τ) is connected by a line to both labels 1 and τ in the Dynkin diagram.

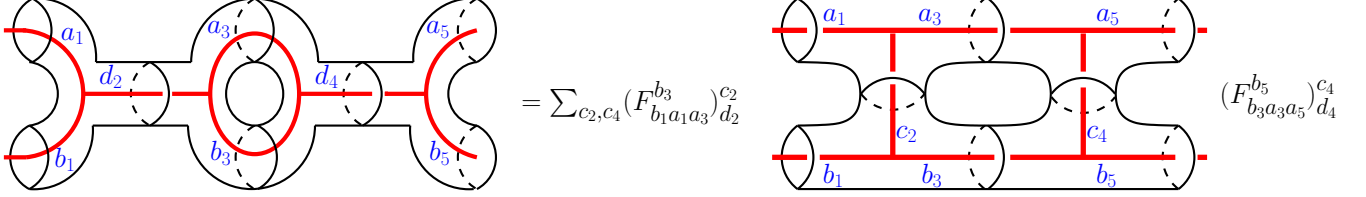


FIG. 18: Two possible basis choices corresponding to different decompositions of the high-genus surface. The basis drawn on the left is used in formulating the exact solution: the rung and the plaquette terms alternatingly act on even or odd ‘sites’ i .

In summary, the elements of this new basis of the Hilbert space on which the Hamiltonian acts are of the form

$$|\vec{\alpha}\rangle := |\dots, \alpha_{i-1}, \alpha_i, \alpha_{i+1}, \dots\rangle, \quad (31)$$

where $\alpha_j [= d_j$ if j is even, and $= (a_j, b_j)$ if j is odd] denotes a point on the D_6 -Dynkin diagram representing the flux through the high-genus surface at the ‘site’ j of the chain. The sequence of α_j must satisfy the condition that α_{j+1} is a nearest neighbor site of α_j on the D_6 -Dynkin diagram.

In this new basis, the rung and plaquette terms H_i^R and H_i^P of our ladder Hamiltonian

$$H = -J_p \sum_{i \text{ odd}} H_i^P - J_r \sum_{i \text{ even}} H_i^R, \quad (32)$$

take on the following form⁴³

$$H_i^P |a_i, b_i\rangle = \sum_{s=1, \tau} \frac{d_s}{D^2} \sum_{a'_i, b'_i} (F_{d_{i+1} b_i s}^{a'_i})_{a_i}^{b'_i} (F_{d_{i-1} a_i s}^{b'_i})_{b_i}^{a'_i} |a'_i, b'_i\rangle, \quad (33)$$

$$H_i^R |d_i\rangle = \sum_{d'_i} (F_{b_{i-1} a_{i-1} a_{i+1}}^{b_{i+1}})_{d_i}^1 (F_{b_{i-1} a_{i-1} a_{i+1}}^{b_{i+1}})_{d'_i}^1 |d'_i\rangle.$$

In fact, these terms can be seen to form a representation of the Temperley-Lieb algebra²⁵ which arises from the D_6 -Dynkin diagram, and has “d-isotopy” parameter $D = \sqrt{1 + \varphi^2} = 2 \cos(\pi/10)$, the total quantum dimension of our Fibonacci theory. Specifically, consider the operators \mathbf{e}_i constructed from the components $v_\alpha = \sin(\alpha\pi/10)$ ($\alpha = 1, \dots, 6$, $v_1 = v_{(1,1)}$, $v_2 = v_{(1)}$, $v_3 = v_{(\tau,\tau)}$, $v_4 = v_{(\tau)}$, $v_5 = v_6 = v_{(1,\tau)} = v_{(\tau,1)}$) of the (‘Perron Frobenius’) eigenvector corresponding to D , the largest positive eigenvalue of the adjacency matrix of the D_6 -Dynkin diagram⁴⁴,

$$\mathbf{e}_i | \dots, \alpha_{i-1}, \alpha_i, \alpha_{i+1}, \dots \rangle := \sum_{\alpha'_i} ((e_i)_{\alpha_{i-1}}^{\alpha_{i+1}})_{\alpha_i}^{\alpha'_i} | \dots, \alpha_{i-1}, \alpha'_i, \alpha_{i+1}, \dots \rangle,$$

$$\text{where} \quad ((e_i)_{\alpha_{i-1}}^{\alpha_{i+1}})_{\alpha_i}^{\alpha'_i} = \delta_{\alpha_{i-1}, \alpha_{i+1}} \sqrt{\frac{v_{\alpha_i} v_{\alpha'_i}}{v_{\alpha_{i-1}} v_{\alpha_{i+1}}}}.$$
 (34)

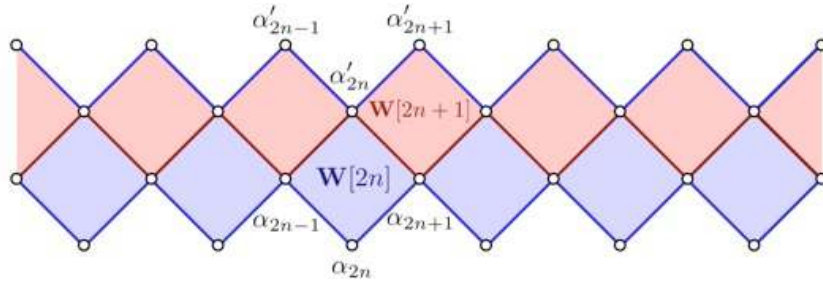
These operators form a known representation²⁴ of the Temperley-Lieb algebra with “d-isotopy”- parameter D , i.e.

$$\mathbf{e}_i^2 = D \mathbf{e}_i, \quad \mathbf{e}_i \mathbf{e}_{i\pm 1} \mathbf{e}_i = \mathbf{e}_i, \quad [\mathbf{e}_i, \mathbf{e}_j] = 0 \quad \text{for } |i - j| \geq 2.$$
 (35)

Now one can check that the rung and plaquette terms, Eq. (33), of the Hamiltonian in the new basis, Eq. (32), are proportional to these operators, i.e.

$$H_i^P = \frac{1}{D} \mathbf{e}_i \quad \text{for } i \text{ odd}, \quad H_i^R = \frac{1}{D} \mathbf{e}_i \quad \text{for } i \text{ even}.$$
 (36)

The Hamiltonian Eq. (33) is in fact that corresponding to the (integrable) restricted-solid-on-solid (RSOS) statistical mechanics lattice model based on the D_6 -Dynkin diagram²⁴. Specifically, the two-row transfer matrix $\mathbf{T} := \mathbf{T}_2 \mathbf{T}_1$ of this lattice model



is written in terms of Boltzmann weights $\mathbf{W}[i]$ assigned to a plaquette i of the square lattice

$$\mathbf{T}_1 := \prod_n \mathbf{W}[2n], \quad \text{and} \quad \mathbf{T}_2 := \prod_n \mathbf{W}[2n+1]$$
 (37)

with

$$\mathbf{W}[i]_{\vec{\alpha}}^{\vec{\alpha}'} = \left\{ \frac{\sin[\frac{\pi}{10} - u]}{\sin \frac{\pi}{10}} \mathbf{1}_{\vec{\alpha}}^{\vec{\alpha}'} + \frac{\sin u}{\sin[\frac{\pi}{10}]} \mathbf{e}[i]_{\vec{\alpha}}^{\vec{\alpha}'} \right\}.$$
 (38)

The parameter $u > 0$ is a measure of the lattice anisotropy, $\mathbf{1}$ is the identity operator, and

$$\mathbf{e}[i]_{\vec{\alpha}}^{\vec{\alpha}'} := \left[\prod_{m \neq i} \delta_{\alpha'_m, \alpha_m} \right] \left((e_i)_{\alpha_{i-1}}^{\alpha_{i+1}} \right)_{\alpha_i}^{\alpha'_i}.$$
 (39)

The Hamiltonian of the so-defined lattice model is obtained from its transfer matrix by taking, as usual⁴⁵, the extremely anisotropic limit, $0 < u \ll 1$,

$$\mathbf{T} = \exp\{-a(\mathbf{H} + c_1) + O(a^2)\}, \quad a = \frac{u}{D \sin[\pi/10]} \ll 1,$$

yielding

$$H = - \sum_i \frac{1}{D} \mathbf{e}_i.$$
 (40)

Since, due to Eq. (36), the operators $\frac{1}{D} \mathbf{e}_i$ are nothing but the rung and plaquette operators, we have thus demonstrated that the Hamiltonian of the RSOS statistical mechanics model based on the Dynkin diagram D_6 coincides with the Hamiltonian, Eq. (32), of our ladder model.

The RSOS model based on D_6 is known^{23,46} to provide an (integrable) lattice realization of the (D, A) modular invariant⁴⁰ of the 7th unitary minimal CFT of central charge $c = 14/15$. In particular, the Hamiltonian of Eq. (2) of the main text at angle $\theta = \pi/4$ will yield the spectrum of that CFT. This exact analytical result is borne out precisely by our numerical (exact diagonalization) studies reported in subsection (II C 1). This CFT with central charge $c = 14/15$ describes the quantum critical point of a 1 + 1 D quantum system, our ladder model. While we cannot make an exact statement for the related 2 + 1 D quantum model, we note that Fendley has recently discussed a 2 + 1 D quantum critical point from a 2 + 0 D perspective¹⁷ by considering a one-parameter family of wavefunctions connecting the ground-state wavefunctions of the two extreme limits of the 2 + 1 D model (1). For a certain value of the parameter he finds a conformal quantum critical point whose ground-state correlators are written in terms of this same $c = 14/15$ CFT.

Another version of this lattice model yielding in the anisotropic limit the negative, $-H$, of the Hamiltonian in Eq. (40) is also integrable and provides⁴⁷ a lattice realization of the Z_8 parafermionic CFT of central charge $c = 7/5$. In particular, the Hamiltonian of Eq. (2) of the main text at angle $\theta = 5\pi/4$ will yield the spectrum of that CFT. Again, this exact analytical result is borne out precisely by our numerical (exact diagonalization) studies reported in subsection (II C 2).

III. THE HONEYCOMB LATTICE MODEL

In this section, we discuss details of the “honeycomb lattice model” whose Hamiltonian is given by Eq. (1) in the paper. We first define the plaquette term of the model and then discuss two limiting phases of the model.

A. The Hamiltonian

In analogy to the plaquette term in the ladder model, Eq. (23), the plaquette term of the honeycomb lattice model (Eq. (1) in the main text) is defined by

$$\delta_{\phi(p),1} \left| \begin{array}{c} a \quad \alpha \quad b \\ \zeta \quad \quad \beta \\ f \quad \quad \quad c \\ \epsilon \quad \quad \quad \gamma \\ e \quad \delta \quad d \end{array} \right\rangle = \sum_{s=1,\tau} \frac{d_s}{D^2} \sum_{\substack{\alpha',\beta',\gamma' \\ \delta',\epsilon',\zeta'}} (F_{a\alpha's}^\zeta)_{\alpha'}^{\zeta'} (F_{f\zeta's}^\epsilon)_{\zeta'}^{\epsilon'} (F_{e\epsilon's}^\delta)_{\epsilon'}^{\delta'} (F_{d\delta's}^\gamma)_{\delta'}^{\gamma'} (F_{c\gamma's}^\beta)_{\gamma'}^{\beta'} (F_{b\beta's}^\alpha)_{\beta'}^{\alpha'} \left| \begin{array}{c} a \quad a' \quad b \\ \zeta' \quad \quad \beta' \\ f \quad \quad \quad c \\ \epsilon' \quad \quad \quad \gamma' \\ e \quad \delta' \quad d \end{array} \right\rangle \quad (41)$$

where the additional two edges of a plaquette are reflected in two additional F -transformations. Again, we can parametrize the coupling constants on a circle as $J_p = \cos(\theta)$ and $J_e = \sin(\theta)$.

B. Excitations

We briefly mention the elementary excitations of this model. In the ‘two-sheets’ phase, which corresponds to couplings $\theta = 0$ ($J_p = 1, J_e = 0$), the elementary excitation is a single plaquette with a τ -flux giving rise to a single ‘hole’ as illustrated on the left in Fig. 19. These excitations are gapped with a gap size of J_p and will delocalize for small couplings $J_e \neq 0$ forming quasiparticle bands. Similar to the ladder model the dispersion of this quasiparticle band can be calculated perturbatively around the ‘two-sheets’ limit.

In the opposite limit of ‘decoupled spheres’, which corresponds to couplings $\theta = \pi/2$ ($J_e = 1, J_p = 0$), the elementary excitation is a ‘plaquette ring’ where all edges around a given plaquette have τ -fluxes, as illustrated on the right in Fig. 19. Again, a perturbative analysis allows to qualitatively describe the quasiparticle band.

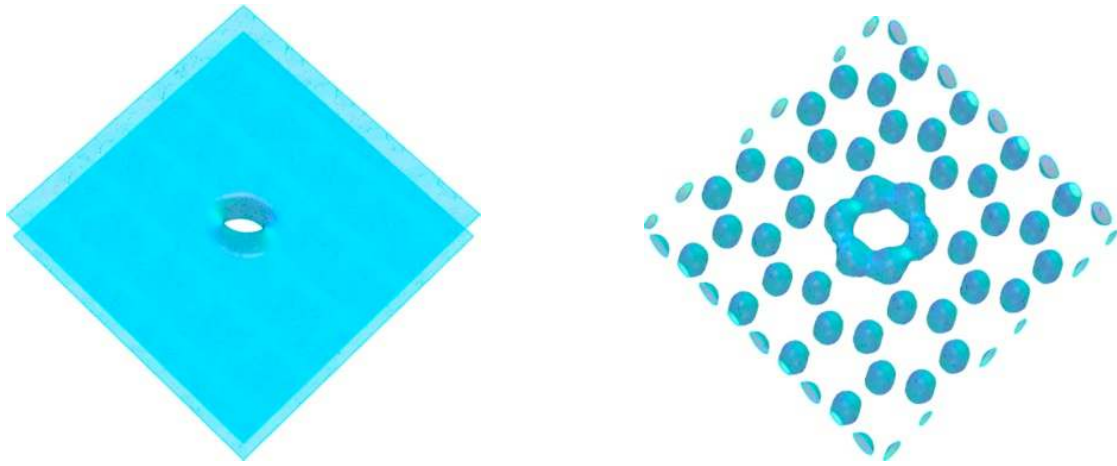


FIG. 19: The elementary excitations above the extreme ground states illustrated in Fig.1 of the main part of the paper: a single plaquette flux in the 'two-sheet' phase, and a single plaquette in the 'multisphere' phase.

-
- ¹ Wen, X.-G. Vacuum degeneracy of chiral spin states in compactified space. *Phys. Rev. B* **40**, 7387 (1989).
- ² Laughlin, R. B. Anomalous Quantum Hall Effect: An Incompressible Quantum Fluid with Fractionally Charged Excitations. *Phys. Rev. Lett.* **50**, 1395 (1983).
- ³ Wen, X.-G., Niu, Q. Ground-State Degeneracy of the Fractional Quantum Hall States in the Presence of a Random Potential and on High-Genus Riemann Surfaces. *Phys. Rev. B* **41**, 9377 (1990).
- ⁴ Moessner, R., Sondhi S. L. Resonating Valence Bond Phase in the Triangular Lattice Quantum Dimer Model. *Phys. Rev. Lett* **86**, 1881 (2001).
- ⁵ Balents, L., Fisher, M. P. A., Girvin, S. M. Fractionalization in an easy-axis Kagome antiferromagnet. *Phys. Rev. B* **65**, 224412 (2002).
- ⁶ L. B. Ioffe *et al.*, Topologically protected quantum bits using Josephson junction arrays. *Nature* **415**, 503 (2002).
- ⁷ Levin, M., Wen, X.-G. String-net condensation: a physical mechanism for topological phases. *Phys. Rev. B* **71**, 045110 (2005).
- ⁸ Kitaev, A. Fault-tolerant quantum computation by anyons. *Ann. Phys.* **303**, 2 (2003).
- ⁹ Kitaev, A. Anyons in an exactly solved model and beyond. *Ann. Phys.* **321**, 2 (2006).
- ¹⁰ Braithwaite, R. S. W., Mereiter, K., Paar, W. H., Clark, A.M. Herbertsmithite, $\text{Cu}_3\text{Zn}(\text{OH})_6\text{Cl}_2$, a new species, and the definition of paratacamite. *Mineral. Mag.* **68**, 527 (2004).
- ¹¹ Okamoto, Y., Hohara, M., Aruga-Katon, H., Takagi, H. Spin-Liquid State in the $S = 1/2$ Hyperkagome Antiferromagnet $\text{Na}_4\text{Ir}_3\text{O}_8$. *Phys. Rev. Lett.* **99**, 137207 (2007).
- ¹² Leinaas, J. M., Myrheim, J. On the Theory of Identical Particles. *Il Nuovo Cimento* **37**, 1 (1977).
- ¹³ Bouwknegt, P. and Schoutens, K. Exclusion statistics in conformal field theory - Generalized fermions and spinons for level-1 WZW theories *Nucl. Phys. B* **547**, 501 (1999).
- ¹⁴ Read, N., Rezayi, E. Beyond paired quantum Hall states: Parafermions and incompressible states in the first excited Landau level. *Phys. Rev. B* **59**, 8084 (1999).
- ¹⁵ Slingerland, J. K. and Bais, F. A. Quantum groups and non-Abelian braiding in quantum Hall systems *Nucl. Phys. B* **612**, 229 (2001).
- ¹⁶ Büchler, H. P., Micheli, A., Zoller, P. Three-body interactions with cold polar molecules. *Nature Phys.* **3**, 726 (2007).
- ¹⁷ Fendley, P. Topological order from quantum loops and nets, *Annals of Physics* **323**, 3113 (2008).
- ¹⁸ Wheeler, J. Geons. *Phys. Rev.* **97**, 511 (1955);
- ¹⁹ Wheeler, J. On the nature of quantum geometrodynamics. *Ann. Phys.* **2**, 604 (1957).
- ²⁰ There exist in fact precisely two CFTs of this central charge. Ours is the non-standard one whose spectrum possesses certain two-fold degeneracies²¹.
- ²¹ Cappelli, A., Itzykson, C., Zuber, J. B. Modular invariant partition functions in two dimensions. *Nucl. Phys. B* **280**, 445 (1987).
- ²² Friedan, D., Qiu, Z., Shenker, S. Conformal Invariance, Unitarity, and Critical Exponents in Two Dimensions. *Phys. Rev. Lett.* **52**, 1575 (1985).
- ²³ Pasquier, V. Lattice derivation of modular invariant partition functions on the torus. *J. Phys. A* **20**, L1229 (1987).
- ²⁴ Pasquier, V. Two-dimensional critical systems labelled by Dynkin diagrams. *Nucl. Phys. B* **285**, 162 (1987).
- ²⁵ Temperley, N., Lieb, E. Relations between percolation and colouring problem and other graph-theoretical problems associated with regular planar lattices - some exact results for percolation problem *Proc. Roy. Soc. Lond. A* **322**, 251 (1971).
- ²⁶ Feiguin, A. *et al.* Interacting Anyons in Topological Quantum Liquids: The Golden Chain. *Phys. Rev. Lett.* **98**, 160409 (2007).
- ²⁷ Gils, C. *et al.* Topological stability of anyonic quantum spin chains and formation of new topological liquids. *Preprint* arXiv:0810.2277 (2008).
- ²⁸ Haldane, F. D. M. "Fractional statistics" in arbitrary dimensions: A generalization of the Pauli principle. *Phys. Rev. Lett.* **67**, 937 (1991).

- ²⁹ Freedman, M., Nayak, C., Shtengel, K. Extended Hubbard Model with Ring Exchange: A Route to a Non-Abelian Topological Phase. *Phys. Rev. Lett.* **94**, 066401 (2005).
- ³⁰ Fradkin, E., Shenker, S. H. Phase diagrams of lattice gauge theories with Higgs fields. *Phys. Rev. D* **19**, 3682 (1979).
- ³¹ Trebst, S., Werner, P., Troyer, M., Shtengel, K., Nayak, C. Breakdown of a Topological Phase: Quantum Phase Transition in a Loop Gas with Tension. *Phys. Rev. Lett.* **98**, 070602 (2007).
- ³² Freedman, M., Nayak, C., Shtengel, K., Walker, K., Wang, Z. A Class of PT-Invariant Topological Phases of Interacting Electrons *Ann. Phys.* **310**, 428 (2004)
- ³³ Albuquerque, A. F. *et al.* The ALPS project release 1.3: Open-source software for strongly correlated systems. *J. of Magn. and Magn. Materials* **310**, 1187 (2007).
- ³⁴ For a pedagogical introduction, we refer to J. Preskill, *Lecture notes on quantum computation*, available online at [http://www.theory-caltech.edu/~preskill/ph229](http://www.theory.caltech.edu/~preskill/ph229).
- ³⁵ A quantum group deformation with deformation parameter q being a root of unity.
- ³⁶ Moore, G., Seiberg, N. Classical and quantum conformal field theory. *Commun. Math. Phys.* **123**, 177-254 (1989).
- ³⁷ which is an extension (truncation) of the $6 - j$ - symbol of $SU(2)$ to the quantum group $SU(2)_q$ for deformation parameter q at root of unity³⁸.
- ³⁸ Kirillov A. N., Reshetikhin, N. Y., in *Infinite dimensional Lie algebras and groups*, (World Scientific, Singapore, 1988).
- ³⁹ Müger, M. From subfactors to categories and topology II: The quantum double of tensor categories and subfactors. *J. Pure Appl. Algebra* **180**, 159-219 (2003).
- ⁴⁰ Cappelli, A., Itzykson, C., Zuber, J.-B. Modular invariant partition-functions in 2 dimensions. *Nucl. Phys.* **B 280**, 445-465 (1987).
- ⁴¹ Freedman, M., Nayak, C., Walker, K., Wang, Z. On Picture (2+1)-TQFTs, *arXiv:0806.1926* (2008).
- ⁴² Zamolodchikov, A. B., Fateev, V. A. Operator algebra and correlation-functions in the two-dimensional $SU(2) \times SU(2)$ chiral Wess-Zumino Model. *Sov. J. Nucl. Phys.* **43**, 657-664 (1986).
- ⁴³ The plaquette term is formulated in the same manner as the one in Eq. 23. The rung term is a projector of the fusion product of anyons a_{i-1} , b_{i-1} , as well as of anyons a_{i+1} and b_{i+1} onto the trivial particle.
- ⁴⁴ This is the matrix whose only non-vanishing matrix elements are $A_{\alpha, \alpha'} = 1$ when α and α' are nearest neighbors on the Dynkin diagram.
- ⁴⁵ Baxter, R. J. *Exactly solved models in statistical mechanics*. (Academic Press, London, 1982).
- ⁴⁶ Pasquier, V. D_n models - local densities. *J. Phys. A* **20**, L221-L226 (1987).
- ⁴⁷ Kuniba, A., Yajima, T. Local state probabilities for solvable restricted solid-on-solid models - A_n , D_n , $D_n(1)$, and $A_n(1)$. *J. Stat. Phys.* **52**, 829-883 (1987).